Experimental Thermal and Fluid Science 82 (2017) 287–301

Contents lists available at ScienceDirect

Experimental Thermal and Fluid Science

journal homepage: www.elsevier.com/locate/etfs

Flow around a circular cylinder with slit

Dong-Lai Gao [a,b], Wen-Li Chen [a,b,*], Hui Li [a,b], Hui Hu [c]

[a] Key Lab of Intelligent Disaster Prevention and Mitigation for Civil Infrastructures, Ministry of Industry and Information Technology, Harbin, Heilongjiang 150090, China
[b] School of Civil Engineering, Harbin Institute of Technology, Harbin, Heilongjiang 150090, China
[c] Department of Aerospace Engineering, Iowa State University, Ames, IA 50011, USA

ARTICLE INFO

Article history:
Received 7 August 2016
Received in revised form 22 November 2016
Accepted 24 November 2016
Available online 25 November 2016

Keywords:
Circular cylinder
Parallel slit
Passive control
Flip-flop

ABSTRACT

Characteristics of flow around a modified circular cylinder are experimentally investigated in the present study. The experimental campaign was performed in a wind tunnel at the Reynolds number of $Re = 2.67 \times 10^4$, based on the cylinder diameter D and the incoming airflow speed. The cylindrical test model is modified with a slit parallel to the incoming airflow to create a flow communicating channel between the windward and leeward stagnation points. The slit width S changes from 0.05 D to 0.15 D with an increment of 0.025 D. Pressure distributions on the cylinder surface were measured to estimate the aerodynamic forces acting on the test model and a particle image velocimetry (PIV) system was employed to quantify the wake flow patterns of the natural and modified cylindrical test models. Experiment results reveal that a slit contributes to reducing the drag and suppressing the fluctuating amplitude of the dynamic wind loads acting on the test model. The changing trend in drag reduction and lift suppression with the increase of slit width are also discussed based on the surface pressure and PIV measurement results. The PIV measurement results demonstrate clearly that the slit generates a self-issuing jet into the cylinder wake and the passive jet is effective in manipulating the wake vortex shedding process from the circular cylinder. As the jet vortices being shifted downstream, they help to detach the shear layers rolled up from both sides of the circular cylinder. Because of this dynamic interaction process, the antisymmetric pattern of the wake vortex shedding from a natural cylinder is found to be converted to a bistable mode flow behind the slotted cylinders. As a result, the dimensionless vortex shedding frequency is observed to be switched to a very low level and a flip-flop phenomenon is found. A linear stability analysis is then performed to suggest that the intrinsic nature of the cylinder wake flow is greatly modified with the implementation of a slit.

1. Introduction

Flow past a bluff body is omnipresent both in nature and many engineering applications. Because of its practical importance in engineering community and significance of understanding fundamental fluid mechanics, flow around a circular cylinder has attracted intensive study interests. When exposed to flow, a circular cylinder is characterized by flow separation and alternating vortex shedding downstream in the near wake [4]. If the circular cylinder is free to oscillate, vortex induced vibrations (VIVs) may take place when its vortex shedding frequency approaches the structure's natural frequency. Engineering structures or equipment with cylindrical cross sections, such as cables of cable-stayed bridges, towers, offshore structures, heat exchangers, are usually immersed in moving fluids (air, water, etc.), thus VIVs are likely to occur. Vortex induced vibrations (VIVs) may lead to catastrophic damages to the structures [9]. Therefore, it is strongly desired to develop effective ways to manipulate the flow and mitigate the potential VIVs.

In consideration of its crucial role in VIVs, a general philosophy adopted in flow control is to attenuate or even completely eliminate the asymmetric vortex shedding from the bluff body. Dong et al. [12] introduced a novel flow control scheme characterized with windward suction and leeward blowing (WSLB) to eliminate the von Kármán street formation in the wake. A complete elimination of the alternating vortex shedding was achieved and the vortex induced cross-flow vibrations were greatly suppressed. Liu and Feng [20] modified a stationary circular cylinder by two synthetic jets positioned at the mean separation points to confirm that a complete suppression of the lift fluctuation on a circular cylinder could be realized by inducing a symmetric vortex shedding mode in the wake. A number of flow control methods have also been

* Corresponding author at: School of Civil Engineering, Harbin Institute of Technology, Harbin, Heilongjiang 150090, China.
E-mail address: cwl_80@hit.edu.cn (W.-L. Chen).

http://dx.doi.org/10.1016/j.expthermflusci.2016.11.025
0894-1777/

proposed to manipulate the wake vortex shedding from a bluff body, reduce the drag and suppress the fluctuating lift. More recently, suction control [7,8], synthetic jets [13–15], plasma actuators [11], heating the cylinder [19], rotating the cylinder [6], electromagnetic force control [24] have been proved to be effective ways to control the flow past a circular cylinder.

These control techniques mentioned above are often referred to as *active control* in the sense that external energy is needed to maintain the control process. Besides active means, *passive control* methods are usually employed to modify the body wake and suppress the resultant flow forces. Efforts have been made by simple modifications to the geometry of the bluff body to improve its fluidic behaviors. Dimpled surface, surface protrusions, groove, splitter plates, and bleed control are typical examples of passive flow control methods, as reviewed in Choi et al. [10]. Zhou et al. [29] experimentally investigated the flow past a circular cylinder with dimpled surface in the Reynolds number range of 7.43×10^3 to 1.798×10^4. The study revealed that the cylinder covered with uniform dimples could reduce the drag coefficient 10% in comparison with a smooth cylinder. Flow structures obtained by PIV technique confirmed that the dimples on the cylinder surface mainly affected the strength of vortex shedding from the cylinder. Owen et al. [23] attached hemispherical bumps to a cylinder surface to reduce the drag and suppress the vortex shedding from a circular cylinder. In their experiment study, the drag reduction was achieved up to 25% and the suppression of vortex shedding has also been recorded for the cylinder with attached bumps. Wu et al. [28] numerically investigated vortex-induced vibration of an elastically mounted circular cylinder with a hinged flat plate. It was found in their study that the cylinder vibration and the force fluctuations could be efficiently suppressed due to the existence of the hinged plate. Meanwhile, the drag force was observed to be reduced significantly and the vortex shedding to become smoother compared to the natural cylinder without plate. Huang [16] carried out experimental investigations to study the effects of triple-starting helical grooves on the fixed circular cylinders and the vortex-induced vibration of elastically supported cylinders. The experiments results demonstrated that for the fixed cylinders, drag reduction was recorded up to 25% in the sub-critical Reynolds number range. When the cylinders were allowed to vibrate freely, the implementation of helical grooves could effectively suppress the vortex-induced cross-flow vibration amplitudes with a substantial amplitude reduction of 64%. Shi and Feng [25] investigated a bleed control of a circular cylinder by forming narrow slots from the windward stagnation point to both the upper and lower separation points. Flow measurement results revealed that the bleed jet interacted with the boundary layer, postponing the separation point to be near the downstream edge of the slot. In consequence, the recirculation bubble located downstream of the circular cylinder is enlarged and the near wake width are increased, resulting in an increased vortex formation length and a decreased vortex shedding frequency.

It can be concluded that a passive control method needs no additional energy input to maintain the control process as long as the control scheme is implemented. In comparison with complex and expensive active techniques, passive control schemes are much easier and less costly from the implementation standpoint and therefore worthy of study. In the present study, a flow communicating channel is created by slotting a slit between the windward and leeward stagnation points of the circular cylinder. Detailed flow measurements are conducted to investigate the flow characteristics around a circular cylinder modified with a slit slotted along the axis. In the context that follows, the test model setup and experimental details are introduced in Section 2, surface pres-

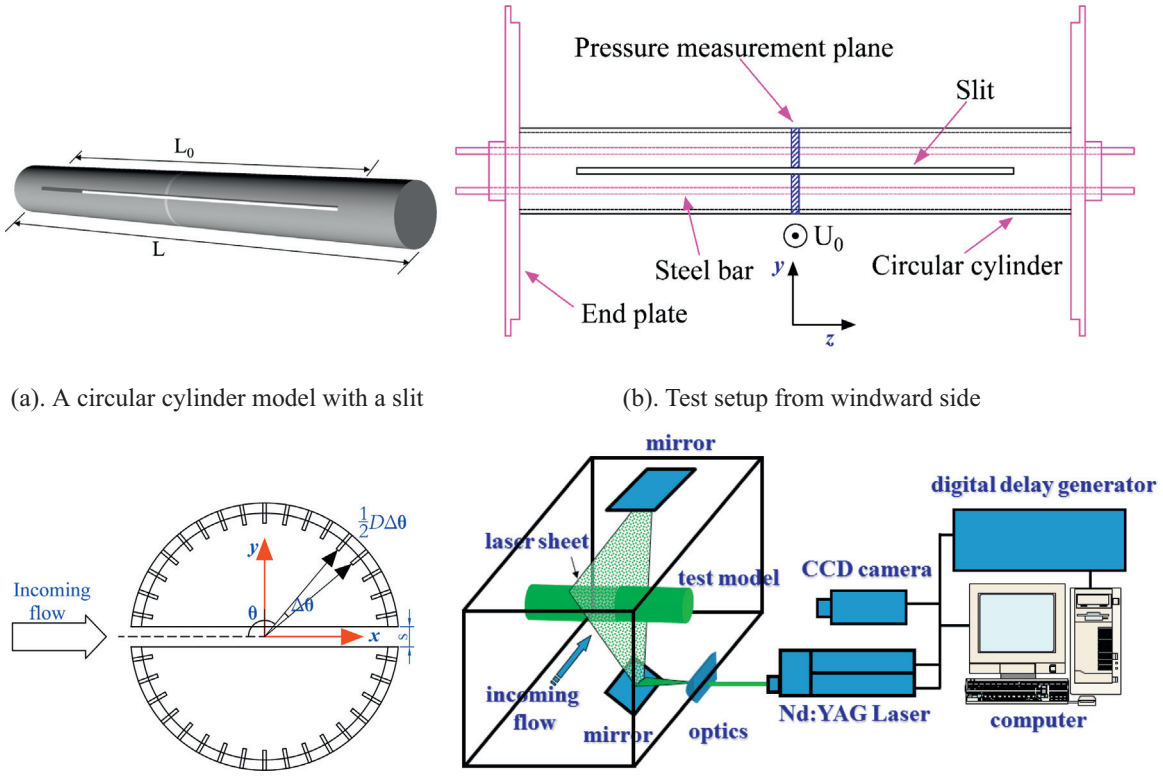

(a). A circular cylinder model with a slit

(b). Test setup from windward side

(c). The pressure measurement plane

(d). PIV system for flow structure measurements

Fig. 1. Schematic views of the test model and experimental setup.

sure measurement and PIV measurement results are presented and discussed in Section 3, followed by some conclusions in Section 4.

2. Test model and experimental setup

The experimental campaign was conducted in a wind tunnel affiliated to the Joint Laboratory of Wind Tunnel and Wave Flume, Harbin Institute of Technology, P. R. China. This closed-circuit wind tunnel has a test section of 505 × 505 mm^2 and the walls of the test section are optically transparent. With honeycombs and mesh structures mounted upstream, a contraction section is installed ahead of the test section to produce uniform incoming flow to enter the test section. The turbulence intensity level in the test section of the wind tunnel was found to be about 0.36%, measured by using a hotwire anemometer.

2.1. A circular cylinder with slit parallel to the incoming airflow

Fig. 1(a) illustrates the cylindrical test models investigated in the present study. The cylindrical test models are made of smooth aluminum alloy tubes with an outer diameter of 50.0 mm. They all have a length L of 503.5 mm, which is determined to adapt to the width of the test section. With longitudinal length L_0 of 400.0 mm, a slit is slotted inside the cylindrical test models to communicate the windward and leeward stagnation points. The width of the slit (S) changes from 2.5 mm to 7.5 mm with the increment of 1.25 mm and the resulting slit ratios (S/D) are 0.05, 0.075, 0.10, 0.125 and 0.15, respectively. The value of L_0/D is calculated to be 8 and the smallest L_0/S 53.33, thus the two-dimensionality of flow round the slotted cylinder is maintained in the mid-span. The cylindrical test models were manufactured by using computer numerical control (CNC) technique to minimize the errors of mechanical process. During the experiments, the slit was set streamwise-oriented, i.e., parallel to the incoming airflow. In addition to the slotted cylinders, a natural cylinder without slit or any other kind of control implementation was also investigated as the baseline case for reference and comparison. During the experiments, the speed of the incoming airflow was set as 8.0 m/s for all the test cases, corresponding to the Reynolds number, based on the diameter of the test model and the incoming airflow velocity, was $Re = 2.67 \times 10^4$.

2.2. Surface pressure distribution measurement in the mid-span

Fig. 1(b) plots the cylindrical model setup in the experiments. The test model was placed horizontally and perpendicularly to the incoming airflow. With two steel bars, the test model was firmly mounted to the end plates, which were locked to the tunnel walls, as shown in Fig. 1(b). No free vibration or flow-induced vibrations has ever been detected during the wind tunnel tests. The slit was always set parallel to the flow direction.

A digital pressure measurement system consisted of 3 models (DSA3217; Scanivalve Corporation, Liberty Lake, Washington) was used to measure the surface pressure distributions in the mid-span of the cylindrical test model. The pressure measurement plane was made of powdered photosensitive resin and manufactured by using a 3D printer. 36 pressure taps were evenly distributed on the pressure measurement plane of the natural cylinder, i.e., the baseline case. It is noteworthy that for the slotted pressure measurement planes, pressure taps are vacant both in windward and leeward stagnation points, as can be seen from Fig. 1(c). With a sampling rate of 312.5 Hz, the data acquisition time for instantaneous surface pressure measurements was set to be 30 s for all the test cases during the wind tunnel tests. Polyvinyl chloride (PVC) tubes with 0.45 m length and 0.9 mm internal diameter were used to connect the pressure taps to the arrayed pressure transducers independently. Based on the findings described in Irwin et al. [17], effects of the tubing system on the surface pressure measurements, such as phase lag of the instantaneous pressure signals and the amplitude attenuation caused by the 0.9-mm-diameter and 0.45-m-long PVC tubing used in the present study were expected to be negligible. However, the solid blockage and the wake blockage effects (the blockage ratio being 9.9%) of the test model on the pressure measurements were corrected, as suggested by Barlow et al. [2].

According to Chen et al. [8], the resultant aerodynamic forces (i.e., the lift and drag forces) acting on the cylindrical test model could be estimated by integrating the measured pressure distributions on the cylinder surface. The coefficients of the lift and drag forces acting on the cylinder, C_L and C_D can be calculated as:

$$C_D = \frac{1}{2}\sum_i C_{p_i} \cdot \Delta\theta_i \cdot \cos\theta_i,$$
$$C_L = \frac{1}{2}\sum_i C_{p_i} \cdot \Delta\theta_i \cdot \sin\theta_i, \quad (1)$$
$$C_{p_i} = \frac{p_i - p_\infty}{\frac{1}{2}\rho U_0^2},$$

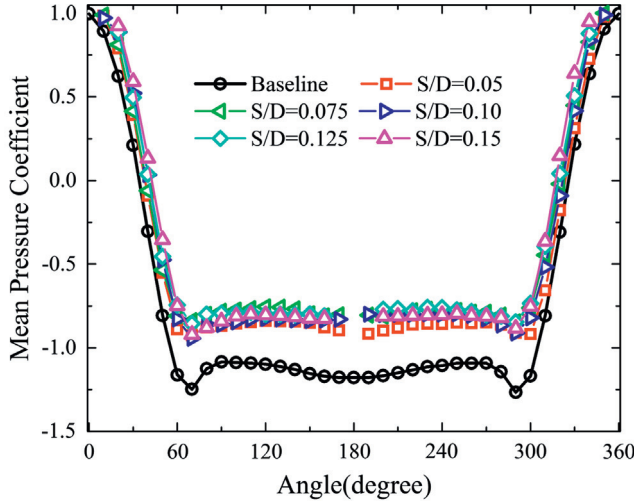

(a) Mean pressure distributions

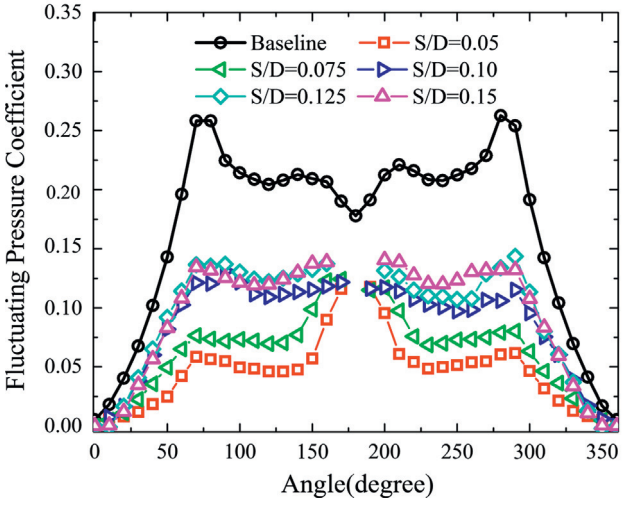

(b) Fluctuating pressure distributions

Fig. 2. Pressure distributions around the circular cylinder model.

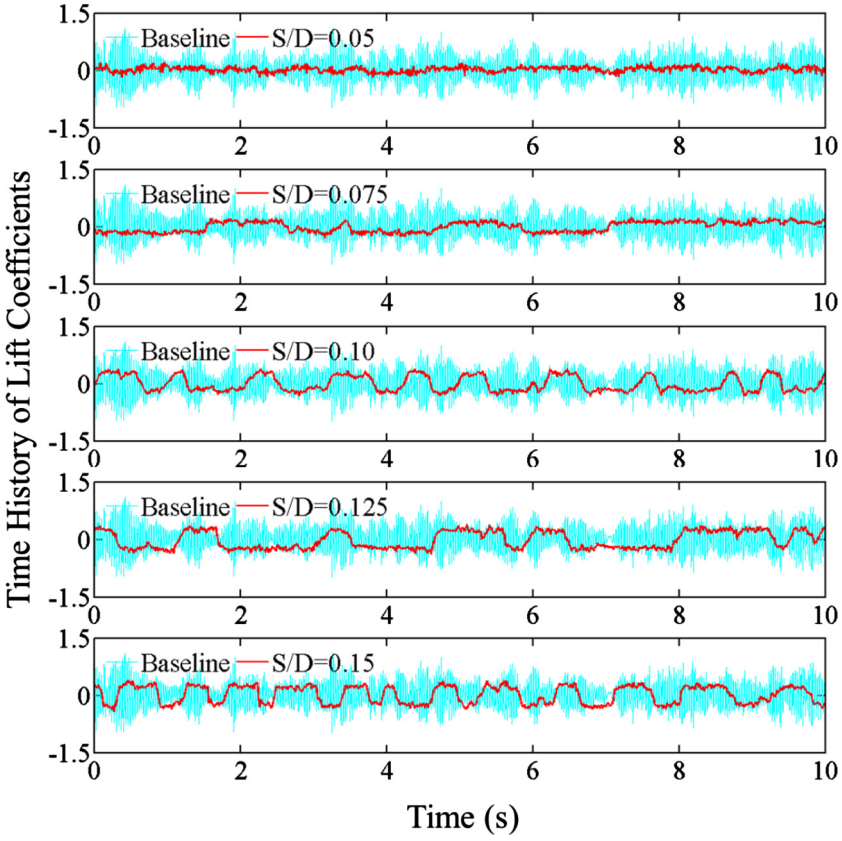

Fig. 3. Time history of the instantaneous lift coefficients.

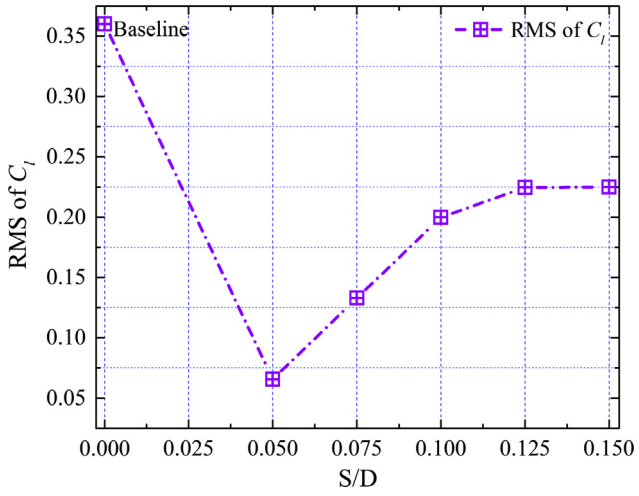

Fig. 4. RMS of the lift coefficients estimated from pressure measurement results.

where C_{p_i} is the surface pressure coefficient on the cylindrical test model, p_i is the static pressure on the cylindrical test model, p_∞ is the static pressure of the incoming flow, time series of p_i and p_∞ are obtained and recorded by the digital pressure measurement system. θ_i is the azimuthal angle of the pressure tap, and $\Delta\theta$ is the angle difference between the two neighboring pressure taps, for the present study, $\Delta\theta = 10°$.

It is worth noting that, the vacancy of pressure taps on the cylinder surface (as shown in Fig. 1(c) has little influence on the estimation of lift forces, because when θ_i is equal to 0° or 180°, $\sin\theta_i$ remains zero. However, cos0° and cos180° are not equal to zero. Therefore, it would be inappropriate to apply Eq. (1) to calculate the drag forces acting on the circular cylinder. The control volume analysis proposed by Bohl and Koochesfahani [5] was employed to estimate the drag coefficients, as will be presented and discussed in Section 3.5.

2.3. PIV system for flow structure measurement

To quantify the flow characteristics around the cylindrical test models modified with and without parallel slit, a high-resolution particle image velocimetry (PIV) system was employed to conduct detailed flow field measurements. Fig. 1(d) shows the schematic of the PIV measurement setup for the flow field measurements. The incoming airflow was seeded with 1–5 μm oil droplets by using a seeding generator. The vertical plane in the mid-span of the test model was illuminated by a double-pulsed Nd:YAG laser adjusted on the second harmonic and emitting two pulses of 200 mJ at the wavelength of 532 nm with a repetition rate of 4 Hz. Manipulated by a set of optics and mirrors, the laser beam was shaped to a thin sheet with a thickness of about 1.0 mm in the target plane. A high-resolution 16-bit CCD camera (PCO 1600, CookeCorp) was used for image acquisition with the axis of the camera being perpendicular to the laser sheet. The CCD camera and double-pulsed Nd:YAG lasers were connected to a host computer via a Digital Delay Generator (Berkeley Nucleonics, Model 575), which controlled the timing of the laser illumination and the image acquisition.

More than 300 frames of instantaneous PIV image pairs were obtained for each case in order to ensure a good convergence of the measurements. After acquiring the PIV images, instantaneous velocity vectors were induced by using frame to frame cross-correlation technique involving successive frames of the patterns of particle images. The size of the interrogation window was

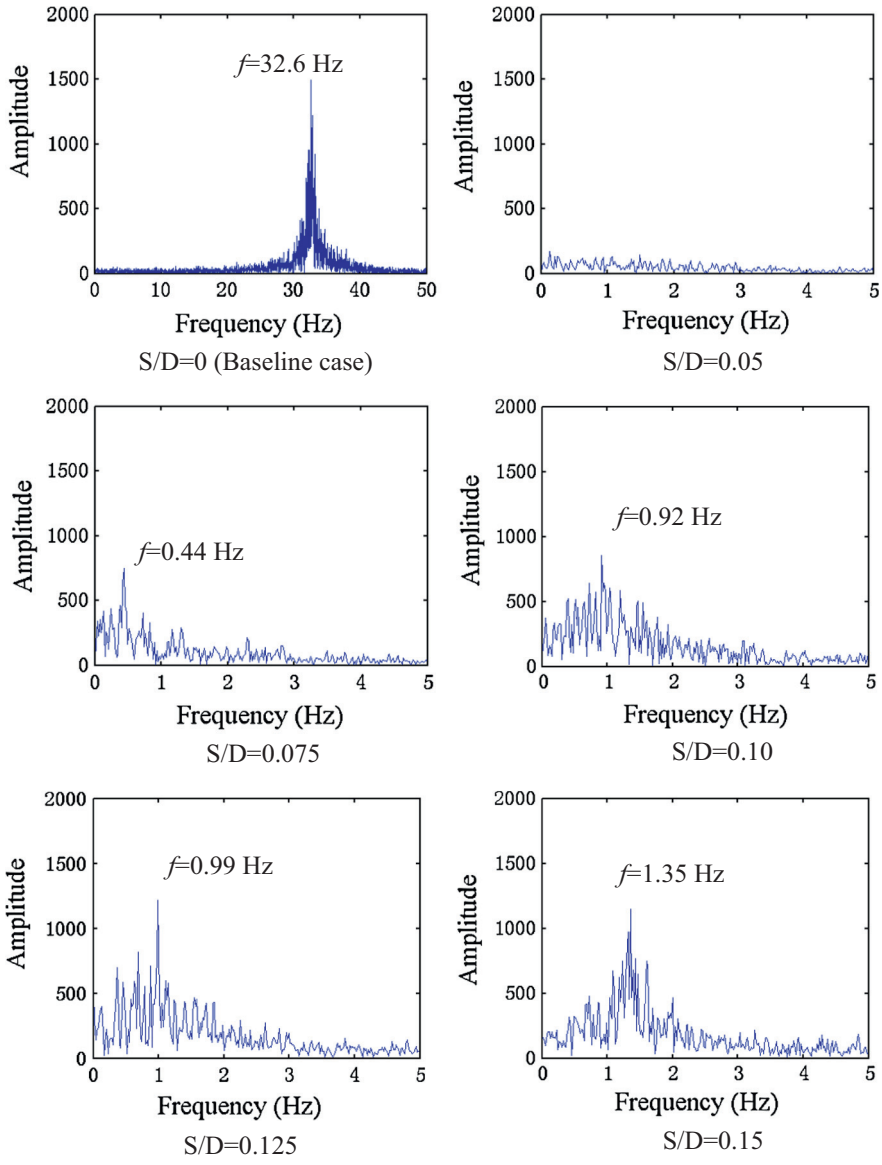

Fig. 5. Frequency spectrum of the lift time histories for different cases.

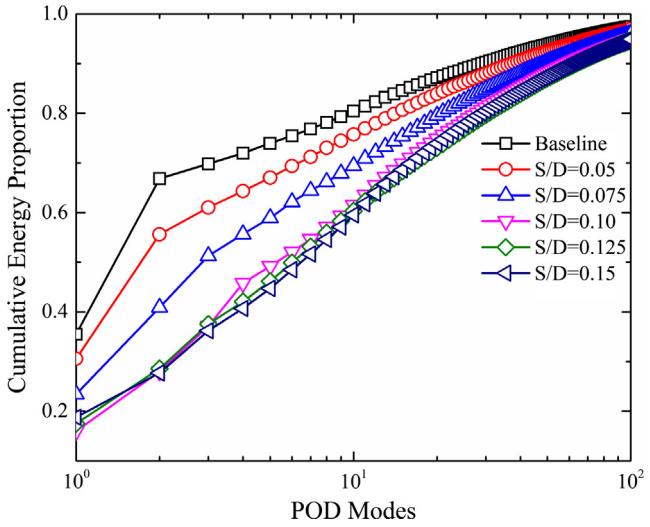

Fig. 6. Cumulative energy proportion versus different POD modes.

32 × 32 pixels and an effective overlap of 50% of the interrogation windows was employed in the PIV image processing. After the instantaneous velocity vectors (u, v) being determined, the instantaneous spanwise vorticity (ω_z) could be derived. The distributions of ensemble-averaged flow quantities, such as the mean velocity (U, V), normalized Reynolds stress $(\bar{\tau} = -\overline{u'v'}/U_0^2)$ and in-plane turbulence kinetic energy $(\mathrm{TKE} = 0.5 \times (\overline{u'^2} + \overline{v'^2})/U_0^2)$, could also be obtained from the instantaneous PIV measurements. For the PIV measurement conducted in the present study, the uncertainty level in the velocity measurement was estimated to be within 2.0%, while the uncertainties for the measurements of ensemble-averaged flow quantities such as the Reynolds stress and turbulent kinetic energy distributions were about 5%.

3. Experiment results

3.1. Pressure distributions and lift forces

Fig. 2 presents the mean and fluctuating pressure distributions on the surface of the cylinder model with and without slit measured by the pressure measurement system. According to the

mean pressure distributions shown in Fig. 2(a), the base pressure regions on the leeward side of the cylinders with slit are clearly lifted in comparison with the baseline case, which indicates a drag reduction for all the controlled cases. The root-mean-square (RMS) values of the instantaneous pressure coefficients are also calculated and presented in Fig. 2(b) to quantify the fluctuation amplitudes of the surface pressure distributions around the circular cylinder. It is found that the pressure fluctuation amplitudes on the leeward side of the test models with slit are much smaller than those of the baseline case. Pressure fluctuations are usually used to evaluate the unsteady wind loads acting on the cylinder. It can therefore be concluded that not only drag reduction but also suppression on the unsteady dynamic wind loads are realized simultaneously by simply slotting a slit in the cylindrical test model.

By applying the formula suggested in Eq. (1), time histories of the lift force coefficients acting on the test model are plotted in Fig. 3. In these subplots, the cyan lines denote the lift coefficients measured from the baseline case, whilst the red lines represent lift coefficients measured from the cylinders with different slit ratios. As can be seen from the figures, the lift coefficients of the natural cylinder without slit experience high magnitudes and significant fluctuations. Nevertheless, the lift forces acting on the cylinder models with slit are all considerably suppressed in comparison with the baseline case.

Root-mean-square (RMS) values of the instantaneous lift coefficients for all test cases (including the natural cylinder and the slotted cylinders) are then calculated and presented in Fig. 4. RMS values of the lift coefficients can be used as a more quantitative approach to assess the effectiveness of flow control. Clearly, a slit can effectively reduce the lift forces acting on the cylindrical test model. It should be noted that for the test case with S/D of 0.05, the RMS value of the lift coefficients reaches a minimum and the lift suppression is found up to 81.78%. This is consistent with the results presented in Figs. 2 and 3. It can be observed in Fig. 2(b) that the pressure fluctuation amplitudes on the leeward side of the cylinder with S/D = 0.05 are distributed on the lower bottom. Moreover, Fig. 3 demonstrates that the lift force coefficients witness the least fluctuation for the test case with S/D of 0.05. The RMS value of the lift coefficients is then found to experience an upward trend with the increase of S/D ratio. When S/D exceeds 0.125, the RMS value of lift coefficients tends to remain stable. It can be concluded that the optimum slit ratio is no larger than 0.05 at the Reynolds number of 2.67×10^4. In the numerical study by Baek and Karniadakis [1], they confirmed that the optimum S/D ratio to obtain the best lift suppression would decrease as the Reynolds number increases. According to their findings, the optimum S/D ratio is 0.16 at the Reynolds number of 500, whilst for the numerical simulations performed at the Reynolds number of 1000, the optimum S/D ratio was found decreased to 0.12. In the present experiment study, we cannot reach a smaller S/D ratio than 0.05 because of the difficulties in mechanical manufacturing. Nevertheless, it is confirmed that an 81.78% lift suppression has been obtained at S/D = 0.05. It should also be noted that in the numerical simulation of Baek and Karniadakis [1], the best lift reduction is less than 80% at the optimum S/D ratio of 0.16.

Fig. 5 shows the results of power spectrum analysis on the measured dynamic lift forces acting on the cylindrical model by using a fast Fourier transform (FFT). As can be seen in these subplots, the baseline case has a dominant frequency of 32.6 Hz and the corresponding Strouhal number ($St = fD/U_0$) is estimated to be 0.204. However, for the time sequences of the lift forces measured from the cylindrical modes with slit, the dominant frequencies in the power spectrum are found to switch to a very small level, as shown in Fig. 5. It indicates a flip-flop phenomenon, during which the switch-over time is one order larger than that of the conventional vortex shedding from a natural cylinder, as reported in the research findings of Kang [18]. In addition, from the frequency spectrum in Fig. 5, it can be observed that the flip-flop switching consists of multiple time scales. The flip-flop phenomenon will be revealed by detailed flow structures measured by PIV system in the following sections.

3.2. Flow structures obtained by PIV measurements

The snapshot proper orthogonal decomposition ('snapshot POD') introduced by Sirovich [26] was adopted for the post processing of the PIV measurement results in the present study. The cumulative energy proportion of the former 100 POD modes to the total one is shown in Fig. 6. For all the test cases, the first few modes occupy most of the energy, as suggested in Meyer et al. [21]. Fig. 7 compares the instantaneous flow around the natural cylinder reconstructed with and without POD modes. It can be seen that the flow structures reconstructed with first 6 POD modes could reflect the dominant flow structures. Based on the energy map of Fig. 6, the flow structures around the cylinders with and without slit are reconstructed by using the first few POD modes.

Fig. 8 shows the instantaneous flow structures of the wake flow behind the cylindrical test model for all test cases obtained by the PIV measurement system. As shown in Fig. 8, a pair of antisymmetric vortex structures are shed from each side of the natural cylinder, i.e., the baseline case, and a Kármán vortex street is observed to form in the wake behind the cylinder. For the cylindrical test models modified with a parallel slit, a pair of symmetric jet

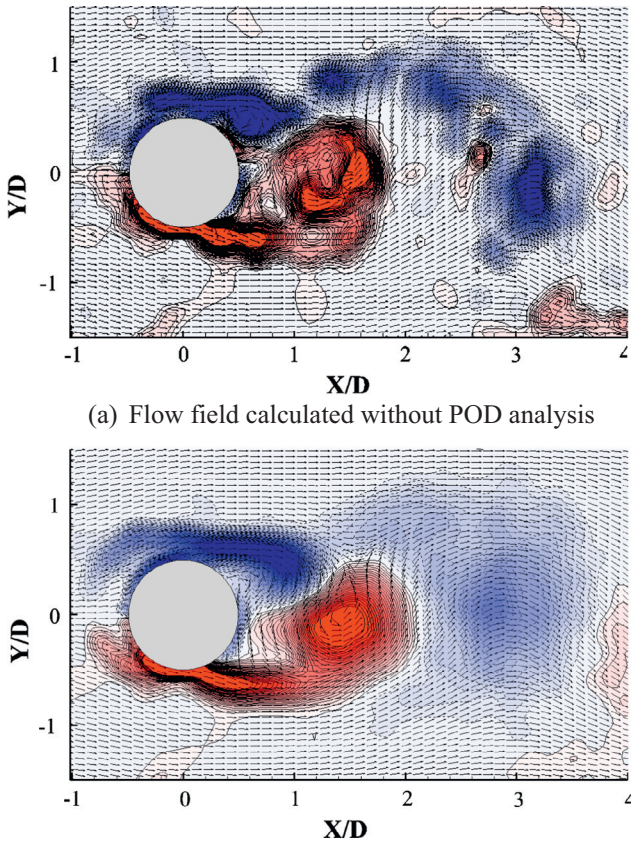

Fig. 7. Flow field reconstructed with and without POD analysis.

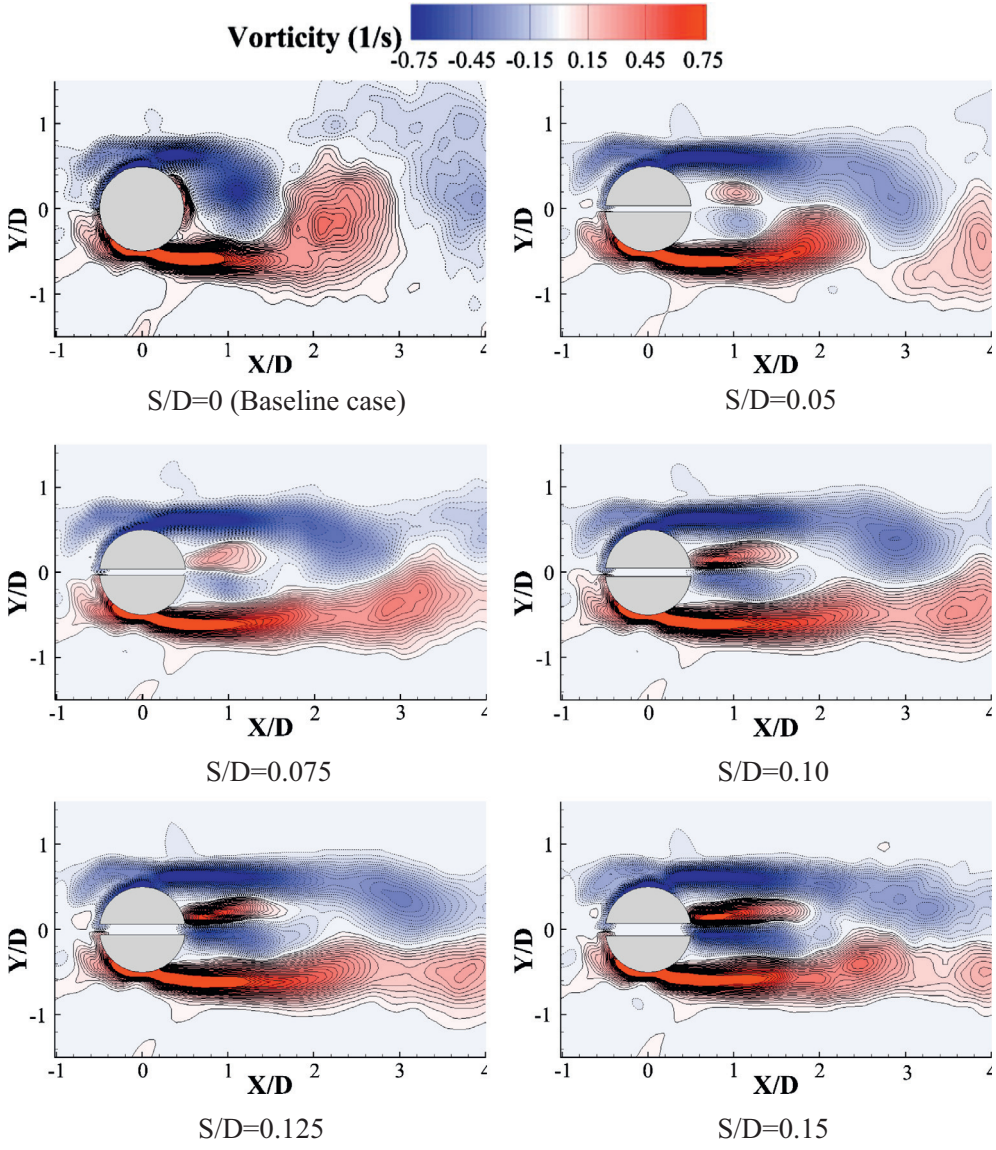

Fig. 8. The instantaneous PIV measurement results in the mid-span plane.

vortices are found to form in the near wake behind the cylindrical test model. A pair of vortices elongates the shear layers rolled up from both sides of the cylinder wall and tends to detach the alternating vortex street. As a result, the vortex formation region is pushed further downstream. It is noteworthy that the jet vortices become stronger with the increase of S/D value, because the self-issuing jet will be strengthened as the slit becomes larger. When S/D >0.10, two arrays of nearly detached wake vortices are observed to form owing to the enhanced jet flow into the wake, which indicates the pattern of the wake vortex shedding has converted into a symmetric mode.

Based on the PIV measurements, the time-averaged flow structures in the mid-span for all test cases are illustrated in Fig. 9. It is shown that a large recirculation region is formed in the wake behind the natural cylinder, i.e., the baseline case. From the time-averaged streamlines behind the slotted cylinder illustrated in Fig. 9, it can be seen that the self-issuing flow jets into the near wake through the orifice placed at the leeward stagnation point, and interacts with the recirculating flow behind the cylinder. For the test case with S/D < 0.10, the interaction and competition between the slit jets and separation flows results in two recirculation regions, an upstream one and a downstream one, in the wake behind the test models. However, when the slit ratio S/D exceeds 0.10, the wake flow patterns of the slotted cylindrical test models behave like two side-by-side arranged D-shaped cylinders. Meanwhile, it can be observed from Fig. 9 that the recirculation bubble length (defined as the length between the cylinder center and the reattachment point) experiences a gradual elongation with the increase of slit width ratio S/D. Besides, the turbulent kinetic energy (T.K.E) values in the wake of the natural cylinder are found to be quite high, especially along the vortex shedding paths, corresponding to the alternate vortex shedding. Benard et al. [3] suggested that the T.K.E values can be used as the measurement of the turbulence mixing in the wake flow. Chen et al. [8] also adopted T.K.E values as an indicator to assess unsteadiness of the surface pressures and the fluctuating amplitude of the resultant dynamic wind loads acting on the cylinder. It is worth noting that the distribution of T.K.E values in the wake behind the slotted cylindrical test models has been greatly modified in comparison with the natural cylinder. In general, the T.K.E levels in the wake flow behind the slotted cylinders are substantially decreased, which indicates a lower turbulence level in the near wake. There-

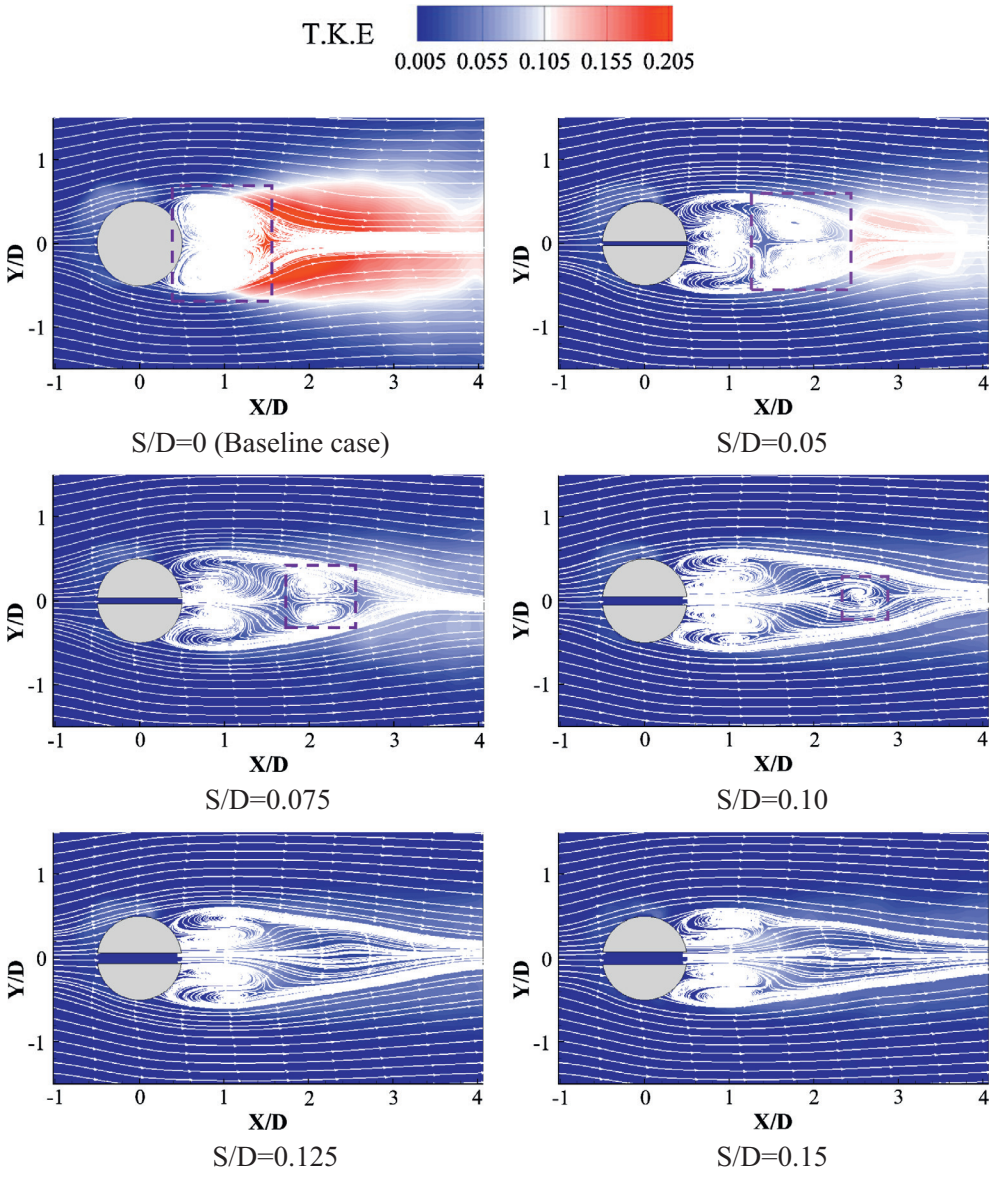

Fig. 9. The time-averaged PIV measurement results in the mid-span plane.

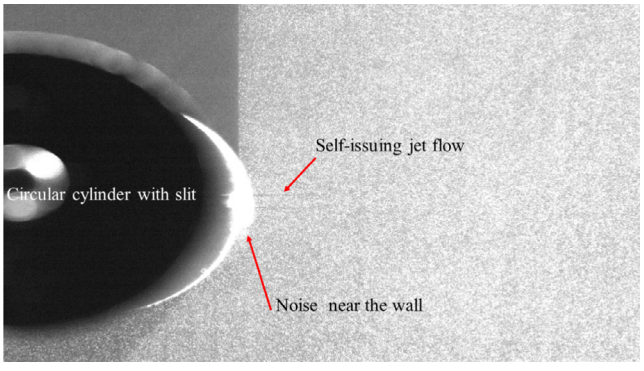

Fig. 10. A raw image taken in the process of PIV measurement.

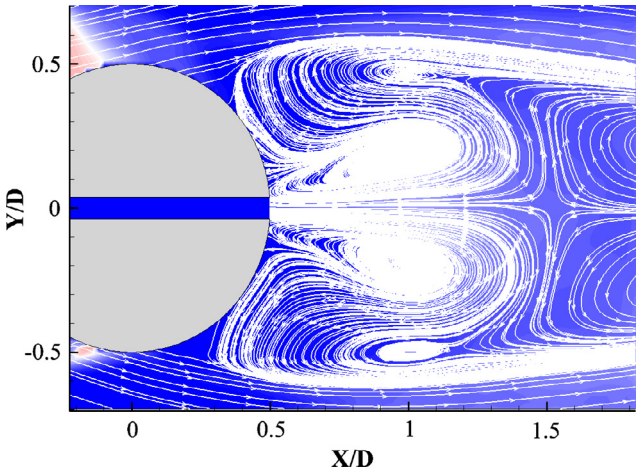

Fig. 11. Time-averaged streamlines in the near wake of the cylinder with S/D = 0.075.

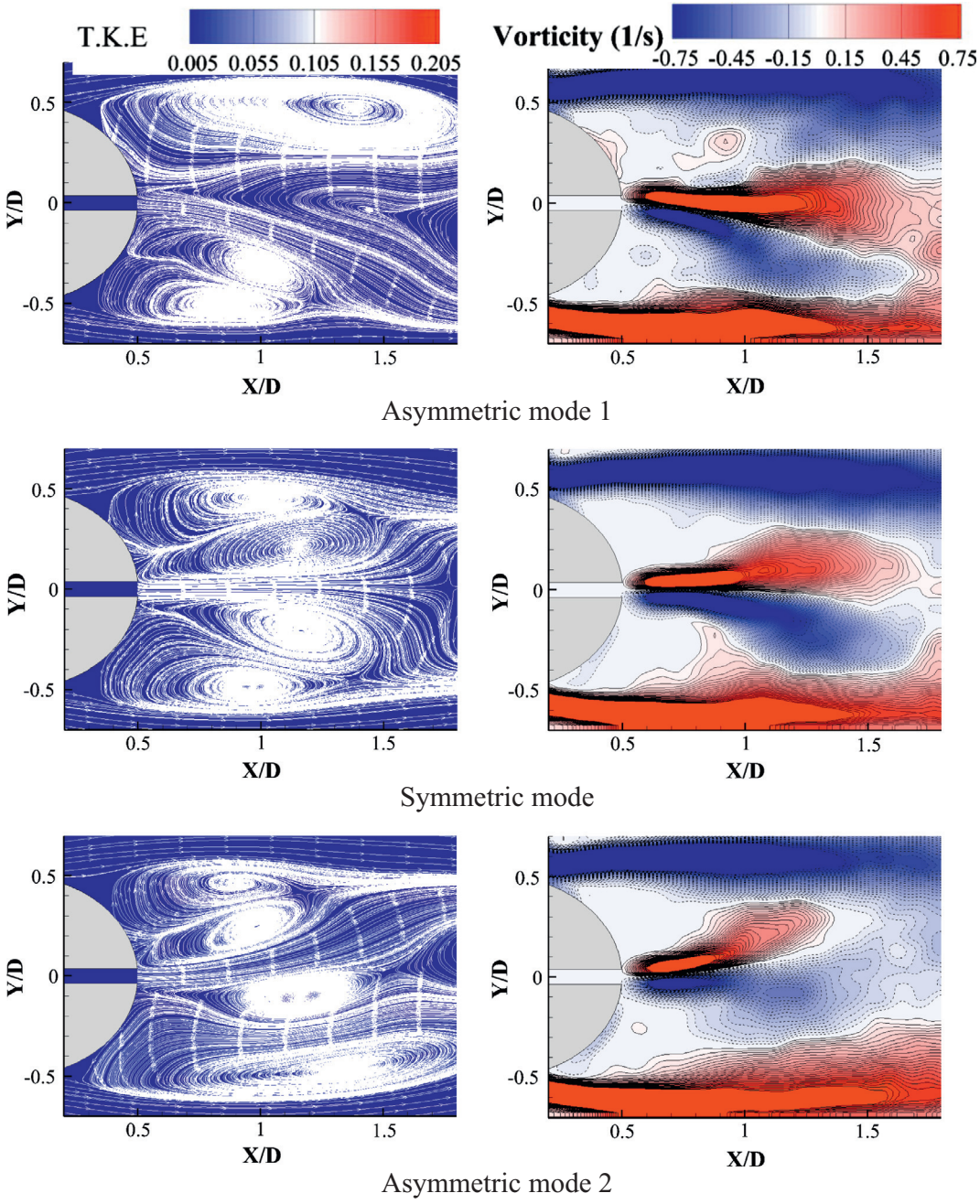

Fig. 12. Typical flow patterns in the very near wake of the cylinder with S/D = 0.075.

fore, the unsteadiness of the surface pressure and the fluctuating amplitude of the resultant dynamic wind loads acting on the test model achieved a suppression in comparison with the baseline case, as shown in Figs. 3 and 4.

3.3. Detailed flow structures behind the cylinder with S/D = 0.075

To get an insight look into the jet and interaction process, a more detailed flow measurement is conducted by using PIV system. The cylindrical test model modified with S/D = 0.075 was selected as the typical case to be investigated. Fig. 10 presents a raw image taken by the high-resolution CCD camera during the PIV measurements. The self-issuing jet flow, characterized with black boundary lines, can be clearly observed to form and blow into the wake region behind the cylindrical test model. The time-averaged streamlines behind the test model with S/D = 0.075 is then induced by using frame to frame cross-correlation with more than 300 pairs of images obtained by PIV system, as shown in Fig. 11. The streamlines exhibits similarity with the results given in Fig. 9, and gives a more detailed look at the upstream recirculation region. When the jet flow is formed and issued into the wake, it competes with the backward flow and is relocated laterally. Afterward, the self-issued jet flow interacts with the shear layers and they are transported downstream together. In consequence, there are two pairs of vortex being observed behind the cylindrical test model, which is different from the pair of vortices formed in the wake of a natural cylinder. The detailed instantaneous flow structures are also presented in Fig. 12. It can be seen that the jet flow is biased towards upward side, downward side or streamwise-oriented intermittently. The jet vortices shed from the slit orifice are expected to be small-scale and symmetric, while the vortices rolled up from the unstable shear layers are essentially

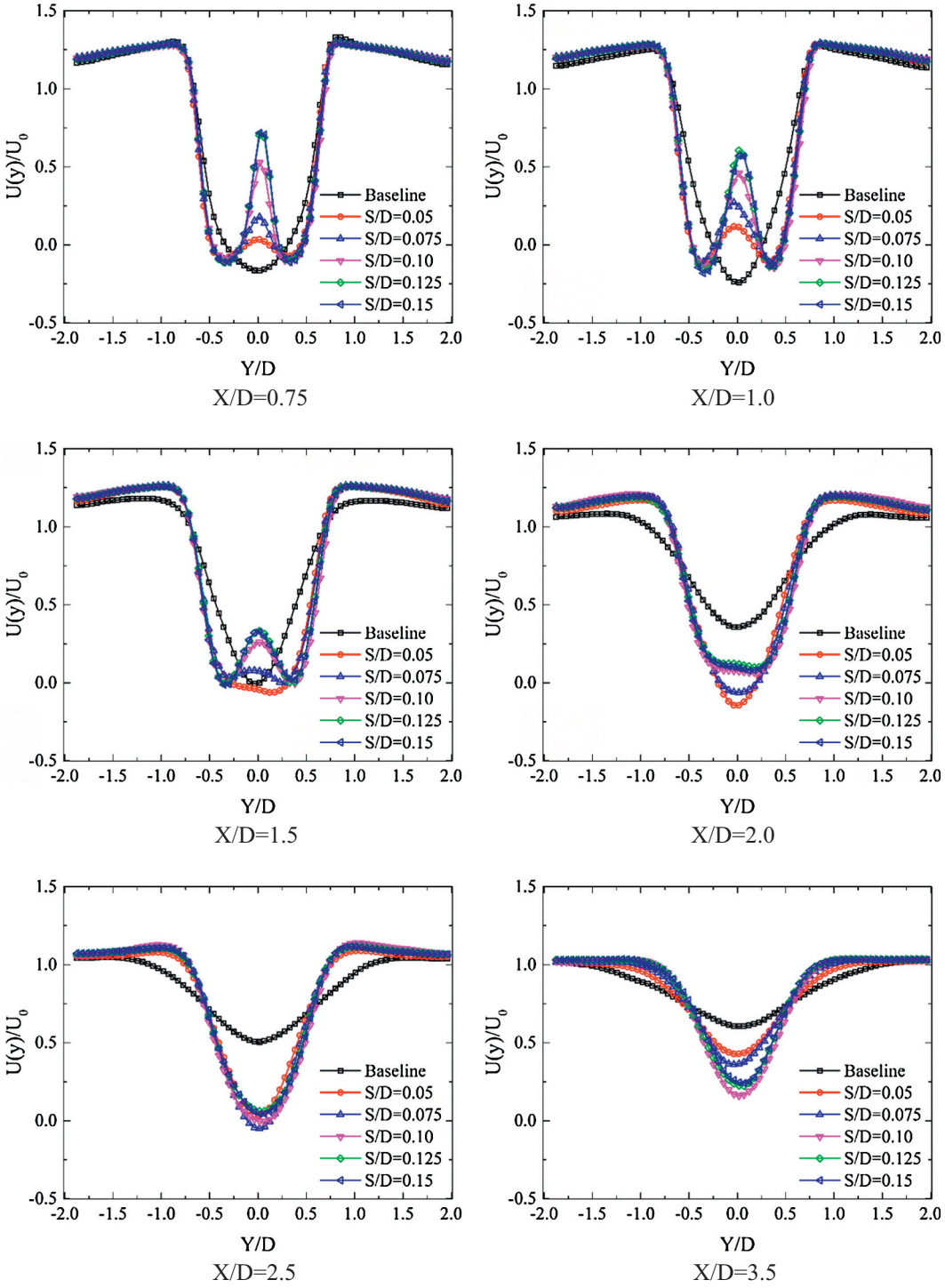

Fig. 13. Profiles of the mean streamwise velocity.

alternating and asymmetric. The competition between the small-scale jet vortices and the asymmetric-mode instability leads to the bistable flow patterns in the near wake. In Fig. 3, the lift force is noticed to switch intermittently for the cylinder with slit, it is also believed to be associated with the flip-flop phenomenon.

3.4. Statistics of the flow field in the cylinder wake

Based on the velocity field obtained by the PIV measurement, some interesting features of the wake flow field can be analyzed. Fig. 13 plots the mean streamwise velocity profiles at different X/D stations (X/D = 0 refers to the center of the cylinder model). It can be seen that, in the near wake region (X/D = 0.75 and 1.0), noticeable cusps can be observed at Y/D = 0 in the velocity profiles behind the cylindrical test models with slit. In general, a larger S/D ratio results in a relatively stronger flow jet into the near wake. When it shifts downstream, the cusps are tends to disappear gradually. In addition, the velocity deficits in the profiles are found to recover gradually as the X/D station goes farther downstream. It should also be noted the velocity deficits behind the slotted

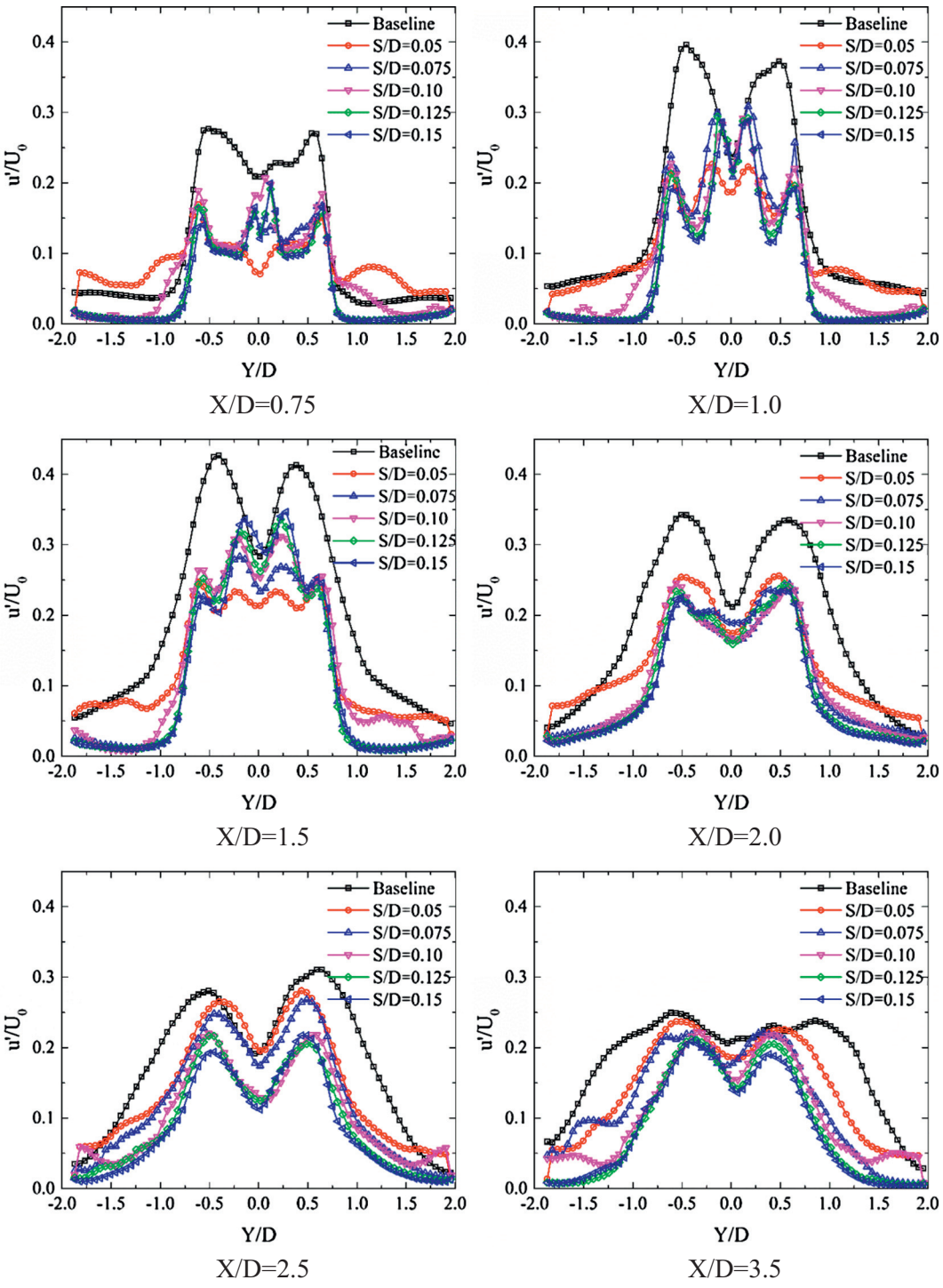

Fig. 14. Profiles of the fluctuating streamwise velocity.

cylinders recover much slower than the baseline case. This is because of the elongation of the recirculation regions, as revealed in the PIV measurement results shown in Fig. 9.

The profiles of the fluctuating streamwise velocity at six different X/D locations are given in Fig. 14. It is observed that the profiles of the natural cylinder exhibit double-cusp patterns, while for the slotted cylinders, their streamwise velocity fluctuation profiles show quadruple-cusp patterns in the near wake (X/D < 2.0). It is associated with the vortex formation process in the upstream recirculation region, as we discussed in Section 3.2. When X/D reaches 2.0 or even larger, the profiles change to double-cusp patterns.

The fluctuating transverse velocity distribution at six different X/D locations are given in Fig. 15. The transverse velocity fluctuation in the wake of slotted cylinders are found to be substantially decreased compared with the baseline case at all of the typical locations. It should be noted that the interaction between the wake vortices is mainly responsible for the transverse velocity fluctuation. Therefore, for the cylindrical test model modified with a slit, the vortex interaction in the wake is greatly suppressed in compar-

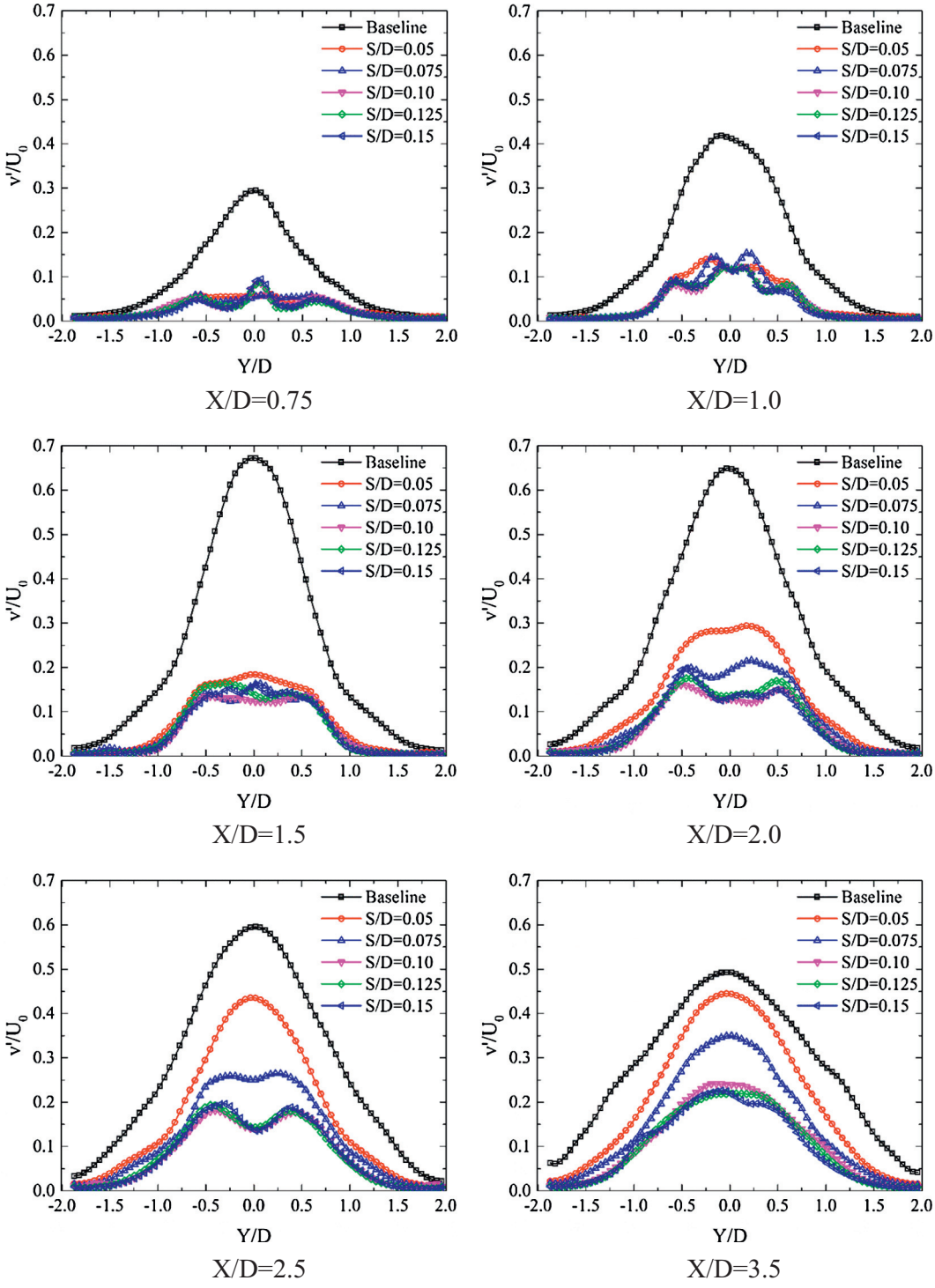

Fig. 15. Profiles of the fluctuating transverse velocity.

ison with the baseline case, which is consistent with the flow structures discussed above. Moreover, the profiles behind the natural cylinder exhibits single-cusp patterns, while the profiles behind the slotted cylinders show more peaks in the near wake.

Fig. 16 presents the distributions of the mean Reynolds stress. For the natural cylinder, a peak and valley with high absolute value of Reynolds stress can be observed around the shear layers in the wake. When it shifts downstream, the peak value reaches a maximum at X/D = 1.5, and then it begins to decrease. For the circular cylinders with slit, the peak values are all greatly decreased at all the X/D locations.

3.5. Drag coefficient estimation

As presented in Section 3.4, the mean velocity fields were obtained by the PIV measurement system. According to the research findings contributed by Bohl and Koochesfahani [5], the mean drag coefficient of the circular cylinder can be estimated by using the following expression:

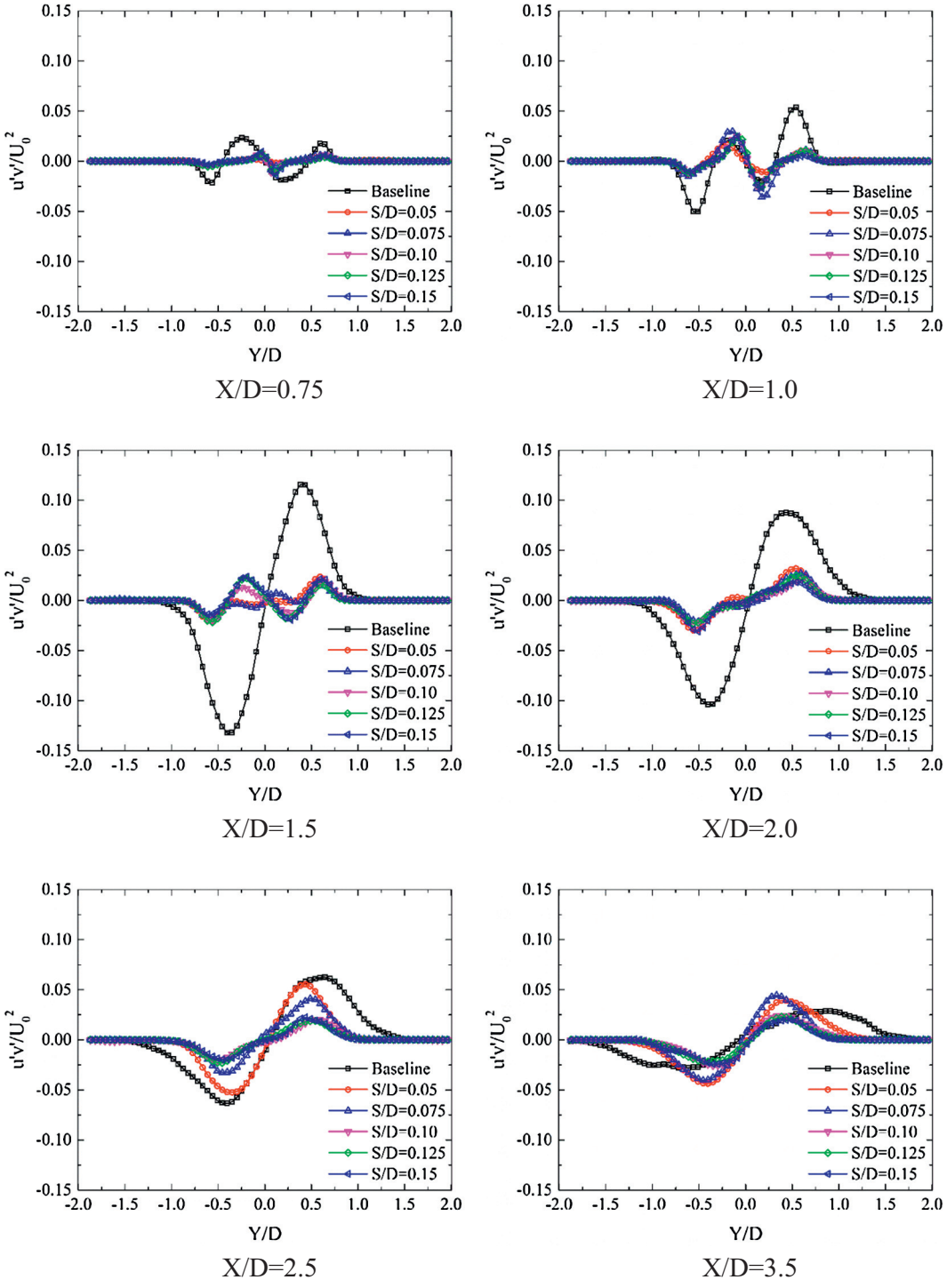

Fig. 16. Reynolds stress distributions.

$$C_D \approx \frac{2}{D}\int_{-H}^{+H}\left\{\frac{U(y)}{U_0}\left(1-\frac{U(y)}{U_0}\right)-\frac{u'^2(y)-v'^2(y)}{U_0^2}+\frac{1}{2}\left(\frac{U_{free}^2}{U_0^2}\right)\right\}dy \quad (2)$$

where $U(y)$ is the mean velocity profile in the wake, $u'(y)$ and $v'(y)$ present the profiles of the streamwise and transverse velocity fluctuations, respectively, U_{free} is the free-stream velocity outside the wake region which is higher than U_0 due to the finite width of the test section, and the last term on the right-hand side accounts for the pressure change in the free stream. The integration interval is from Y/D = −2.0 to 2.0. Applying this formula, the mean drag coefficients of the test cylinder model are analyzed to assess the effects of the slit slotted in the cylinder. The drag estimation results are given in Fig. 17. The mean drag coefficient of the natural cylinder is estimated to be 1.14, which is consistent with the result derived from Eq. (1) based on pressure measurement results. It can be seen from Fig. 17 that with the implementation of cylinder slit, the mean drag coefficient experiences a downward trend in comparison with the natural cylinder. At S/D = 0.05, the drag

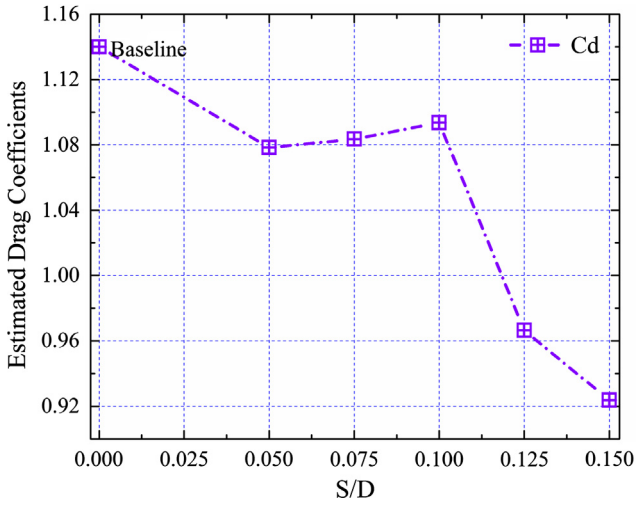

Fig. 17. Drag coefficients estimated from the flow field results.

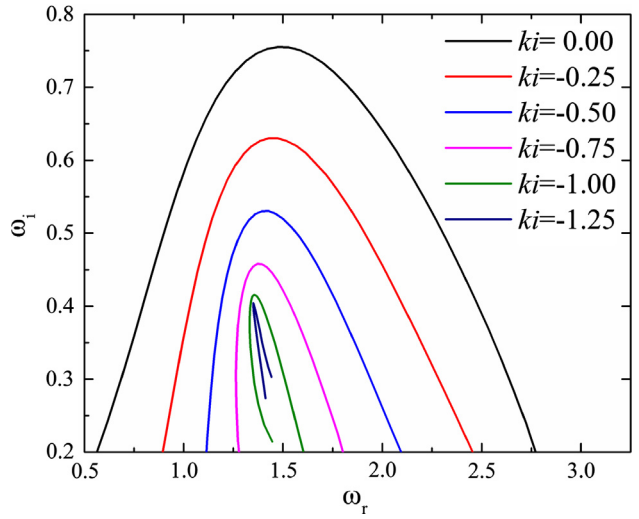

Fig. 18. Map of lines k_i = constant in the ω plane, at X/D = 0.75 for the baseline case.

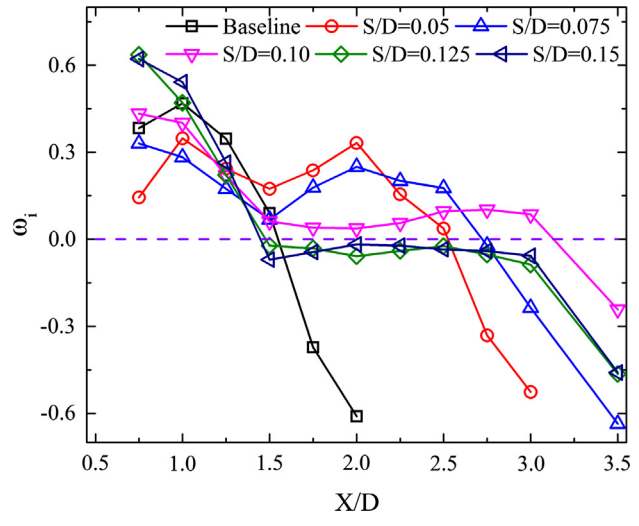

Fig. 19. Imaginary part of the critical point versus X/D for various test cases.

reduction is found to be 6.14%.When the slit width increases, the mean drag coefficient experiences a slight increase and then shifts downwards again after S/D = 0.10. One possible explanation is that the flip-flop flow has been gradually developed with the increase of slit width and the effects of passive jets become weak. When S/D changes to 0.15, the drag reduction is found up to be 18.42%.

3.6. Linear stability analysis

As suggested in Triantafyllou et al. [27], the absolute instability of the wake behind the circular cylinder is responsible for the vortex formation behind a stationary cylinder. Based on the time-averaged streamwise velocity profiles, the Orr-Sommerfeld equation was solved to determine the stability nature of the wake profile and the vortex formation characteristics. Orszag [22] firstly proposed the expansions in Chebyshev polynomials to solve Orr-Sommerfeld equation and very satisfactory results were obtained. The numerical solutions in the present study were based on the method proposed by Orszag [22] and Triantafyllou et al. [27]. The dispersion relation $\omega = \omega(k)$ maps k_i constant lines on the ω plane at different downstream locations. For different k_i, a bunch of quadratic maps with similar shape can be obtained. The maps touch at the critical point with a coordinate of (ω_r, ω_i). The nature of the instability is determined by the imaginary part of the complex frequency at the critical point, i.e., ω_i. A positive ω_i supports an absolute instability, whilst a negative ω_i will support a convective instability, as suggested in Triantafyllou et al. [27].

Fig. 18 gives a map of lines (k_i=constant) in the ω plane, where k is the complex wave number and k_i denotes its imaginary part. The Orr-Sommerfeld equation was solved to plot Fig. 18 based on the time-averaged velocity profile behind the natural cylinder at the downstream location of X/D = 0.75. The mapped curves touch at the critical point, which looks like a cusp on the plane. As can be seen from Fig. 18, the imaginary part of the critical point is 0.40, while its real part (ω_r) is 1.33. Therefore, the mean velocity profile of the wake flow behind the natural cylinder at the downstream location of X/D = 0.75 supports an absolute instability, which leads to the formation of vortex in the near wake. In addition, the corresponding Strouhal number (St) can be derived from the critical value of ω_r by $St = \omega_r/2\pi = 0.21$, which agrees well with the non-dimensional vortex shedding frequency obtain by the power spectrum analysis of the measured dynamic lift forces acting on the test model (i.e., $St = fD/U_0 = 0.204$).

Fig. 19 illustrates the ω_i values at different downstream locations for all test cases. It can be seen that with the increase of slit width, the results of linear stability analysis show a great modification in the wake flow. In the immediate wake (i.e., the region of X/D = 0.75), the disturbance growth rate ω_i is found to decrease with a slit ratio of S/D = 0.05. However, the ω_i value at the station of X/D = 0.75 witnesses a gradual increase as the slit becomes wider. This may partly explain the changing trend of lift forces acting on the test models, as illustrated in Fig. 4. For the natural cylinder, the absolute instability zone is confined to the near wake, i.e., X/D < 1.5, and the ω_i value at X/D = 0.75 is high. In Fig. 9, the center of vortices behind the natural cylinder is observed near the station of X/D = 0.75. The local peak values of ω_i predict the maximum local growth rates, which is associated to the center of vortices formed in the wake, as suggested in Baek and Karniadakis [1]. Therefore, Fig. 19 also reflects the evolution of vortex formation in the near wake as the slit width increases. It can be seen that two absolute instability pockets, though separated by a small valley, can be observed in the near wake for the test cases of S/D = 0.05, 0.075 and 0.10. As we noticed in Fig. 9, two vortex systems are formed in the wake region of these cases, one is attached to the rear wall of the cylindrical test model and the other is

located farther downstream. Their vortex center locations are reflected by the peak values of ω_i in Fig. 19. Besides, the downstream absolute instability pockets in Fig. 19 for the test cases of S/D >0.10 are no longer noticeable because they only have one vortex system near the cylinder wall. It should also be noted that for the cylinders with S/D larger than 0.125, their wake flows are found to be converted into convective instability after the downstream location of X/D = 1.5.

4. Conclusions

Flow past a modified circular cylinder with a slit was experimentally investigated at a Reynolds number of $Re = 2.67 \times 10^4$ in the present study. The slit was manufactured inside the cylinder and was set parallel to the incoming airflow to create a flow communicating channel between the windward and leeward stagnation points.

Based on the surface pressure the RMS value of lift forces acting on the circular cylinder with a slit ratio of S/D = 0.05 is suppressed up to 81.78% in comparison with the natural cylinder. As the slit ratio increases, the lift coefficient experiences an upward trend. By employing control volume analysis, the mean drag coefficients are also estimated based on mean velocity profiles obtained by PIV measurement. It is found that with the increase of slit width, the mean drag coefficient decreases gradually until it remains stable when S/D exceeds 0.125. At S/D = 0.125, the best drag reduction is achieved up to 14.64%.

For the cylindrical test models modified with a slit parallel to the incoming airflow, a pair of symmetric jet vortices are found to form in the near wake behind the cylinder. The vortices interacts with and elongates the shear layers rolled up from both sides of the cylinder wall and tends to detach the alternating vortex street. When S/D >0.10, two arrays of nearly symmetric wake vortices are observed to form in the wake and the vortex formation region is pushed further downstream. In addition, the distribution of T.K.E in the wake behind the slotted cylindrical test models has been greatly suppressed in comparison with the natural cylinder. For the test cases with S/D < 0.10, two recirculation regions are observed to form behind the test model because of the interaction between the self-issued jets and the separation flows. When the slit ratio S/D exceeds 0.10, the wake flow patterns of the slotted cylindrical test models behave like two side-by-side arranged D-shaped cylinders. The recirculation bubble length experiences a gradual elongation with the increase of S/D value.

Detailed flow structures behind the cylinder with S/D = 0.075 reveal that the competition between the symmetric-mode jet vortices and the asymmetric-mode shear layer instability result in bistable flow patterns in the near wake. A linear stability analysis is performed to suggest that the wake flow is greatly modified by the slit slotted in the cylindrical test model and the double-peak absolute ω_i pockets are responsible for the formation of two vortex systems formed in the wake of cylinders with slit ratio of S/D = 0.05, 0.075 and 0.10.

Acknowledgements

This research work is funded by the National Natural Science Foundation of China (NSFC 51378153, 51578188, 51008093, 51161120359 and 91215302) and the Fundamental Research Funds for the Central Universities (HIT. BRETIII. 201512).

References

[1] H. Baek, G. Karniadakis, Suppressing vortex-induced vibrations via passive means, J. Fluids Struct. 25 (5) (2009) 848–866.
[2] B. Barlow, H. Rae, A. Pope, Low-Speed Wind Tunnel Testing, third ed., Wiley, New York, 1999, pp. 330–375.
[3] N. Benard, N. Balcon, G. Touchard, E. Moreau, Control of diffuser jet flow: turbulent kinetic energy and jet spreading enhancements assisted by a non-thermal plasma discharge, Exp. Fluids 45 (2008) 333–355.
[4] D. Brika, A. Laneville, Vortex-induced vibrations of a long flexible circular cylinder, J. Fluid Mech. 250 (1993) 481–508.
[5] D. Bohl, M.M. Koochesfahani, MTV measurements of the vortical field in the wake of an aerofoil oscillating at high reduced frequency, J. Fluid Mech. 620 (2009) 63–88.
[6] A.S. Chan, P.A. Dewey, A. Jameson, et al., Vortex suppression and drag reduction in the wake of counter-rotating cylinders, J. Fluid Mech. 679 (2011) 343–382.
[7] W.L. Chen, D.B. Xin, F. Xu, H. Li, J.P. Ou, H. Hu, Suppression of vortex-induced vibration of a circular cylinder using suction-based flow control, J. Fluids Struct. 42 (2013) 25–39.
[8] W.L. Chen, H. Li, H. Hu, An experimental study on a suction flow control method to reduce the unsteadiness of the wind loads acting on a circular cylinder, Exp. Fluids 55 (4) (2014) 1–20.
[9] W.L. Chen, Q.Q. Zhang, H. Li, H. Hu, An experimental investigation on vortex induced vibration of a flexible inclined cable under a shear flow, J. Fluids Struct. 54 (2015) 297–311.
[10] H. Choi, W.P. Jeon, J. Kim, Control of flow over a bluff body, Annu. Rev. Fluid Mech. 40 (2008) 113–139.
[11] T.C. Corke, C.L. Enloe, S.P. Wilkinson, Dielectric barrier discharge plasma actuators for flow control, Annu. Rev. Fluid Mech. 42 (2010) 505–529.
[12] S. Dong, G.S. Triantafyllou, G.E. Karniadakis, Elimination of vortex streets in bluff-body flows, Phys. Rev. Lett. 100 (20) (2008) 204501.
[13] L.H. Feng, J.J. Wang, C. Pan, Effect of novel synthetic jet on wake vortex shedding modes of a circular cylinder, J. Fluids Struct. 26 (2010) 900–917.
[14] L.H. Feng, J.J. Wang, Circular cylinder wake vortex synchronization control with synthetic jet positioned at back stagnation point, J. Fluid Mech. 662 (2010) 232–259.
[15] L.H. Feng, J.J. Wang, Synthetic jet control of separation in the flow over a circular cylinder, Exp. Fluids 53 (2012) 467–480.
[16] S. Huang, VIV suppression of a two-degree-of-freedom circular cylinder and drag reduction of a fixed circular cylinder by the use of helical grooves, J. Fluids Struct. 27 (7) (2011) 1124–1133.
[17] H. Irwin, R. Cooper, R. Girard, Correction of distortion effects caused by tubing systems in measurements of fluctuating pressures, J. Wind Eng. Ind. Aerodyn. 5 (1) (1979) 93–107.
[18] S. Kang, Characteristics of flow over two circular cylinders in a side-by-side arrangement at low Reynolds numbers, Phys. Fluids 15 (2003) 2486.
[19] J.C. Lecordier, L. Hamma, P. Parantheon, The control vortex shedding behind heated cylinders at low Reynolds numbers, Exp. Fluids 10 (1991) 224–229.
[20] Y.G. Liu, L.H. Feng, Suppression of lift fluctuations on a circular cylinder by inducing the symmetric vortex shedding mode, J. Fluids Struct. 54 (2015) 743–759.
[21] K.E. Meyer, J.M. Pedersen, O. Özcan, A turbulent jet in crossflow analysed with proper orthogonal decomposition, J. Fluid Mech. 583 (2007) 199–227.
[22] S.A. Orszag, Accurate solution of the Orr-Sommerfeld stability equation, J. Fluid Mech. 50 (4) (1971) 689–703.
[23] J.C. Owen, P.W. Bearman, A.A. Szewczyk, Passive control of VIV with drag reduction, J. Fluids Struct. 15 (3) (2001) 597–605.
[24] O. Posdziech, R. Grundmann, Electromagnetic control of seawater flow around circular cylinders, Eur. J. Mech.-B/Fluids 20 (2) (2001) 255–274.
[25] X.D. Shi, L.H. Feng, Control of flow around a circular cylinder by bleed near the separation points, Exp. Fluids 56 (12) (2015) 1–17.
[26] L. Sirovich, Turbulence and the dynamics of coherent structures. Part I: coherent structures, Quart. Appl. Math. 45 (3) (1987) 561–571.
[27] G. Triantafyllou, M. Triantafyllou, C. Chryssostomidis, On the formation of vortex streets behind stationary cylinders, J. Fluid Mech. 170 (1986) 461–477.
[28] J. Wu, C. Shu, N. Zhao, Numerical investigation of vortex-induced vibration of a circular cylinder with a hinged flat plate, Phys. Fluids (1994-present) 26 (6) (2014) 063601.
[29] B. Zhou, X. Wang, W. Guo, W.M. Gho, S.K. Tan, Control of flow past a dimpled circular cylinder, Exp. Therm. Fluid Sci. 69 (2015) 19–26.